Article

Unraveling the doping mechanisms in lithium iron phosphate

Bo Zhang, Yufang He, Hongqiang Gao, Xiaodan Wang, Jinli Liu, Hong Xu*, Li Wang*, Xiangming He*

Institute of Nuclear and New Energy Technology, Tsinghua University, Beijing 100084, China.

***Correspondence to:** Prof./Dr. Xiangming He, Institute of Nuclear and New Energy Technology, Tsinghua University, 30 Shuangqing Road, Haidian District, Beijing 100084, China. E-mail: hexm@tsinghua.edu.cn; Prof./Dr. Li Wang, Institute of Nuclear and New Energy Technology, Tsinghua University, 30 Shuangqing Road, Haidian District, Beijing 100084, China. E-mail: wang-l@tsinghua.edu.cn; Prof./Dr. Hong Xu, Institute of Nuclear and New Energy Technology, Tsinghua University, 30 Shuangqing Road, Haidian District, Beijing 100084, China. E-mail: hongxu@tsinghua.edu.cn

Abstract

As a result of the extensive research and application of LiFePO$_4$ (LFP) in the past > 20 years, there is now a relatively in-depth understanding of its structural stability, phase transition mechanism and electrochemical properties. However, the difficulties faced by further improving the performance of LFP due to its intrinsic low electronic and ionic conductivity have not yet been effectively solved. In order to unlock the effect of transition metal doping on the physicochemical properties of LFP, we establish doping models for all 3d, 4d and 5d transition metals in LFP and compare and analyze their structural properties, band gaps, formation energies, elastic properties, anisotropies and lithiation/delithiation voltages using ab-initio computational screening. According to our screening results, the V-, Mn-, Ni-, Rh- and Os-doped LFP structures have excellent electrochemical properties and can be used as high-performance cathode materials for Li-ion batteries.

Keywords: LiFePO$_4$, doping, computational screening, stability, cathode materials, lithium-ion batteries

INTRODUCTION

Olivine-type LiFePO$_4$ (LFP) was first proposed as a cathode for lithium-ion batteries (LIBs) in 1997 by J. B. Goodenough, a Nobel Prize winner for Chemistry in 2019[1]. Subsequently, LFP has been the focus of

significant research because of its high theoretical capacity (170 mAh·g⁻¹), good stability, high safety and environmental friendliness[2-6]. Currently, LFP is mainly used in electric vehicles, hybrid electric vehicles and communication backup power supplies[7-10]. However, its poor electronic and lithium-ion conductivities represent bottlenecks that limit its further applications[11-13].

To further improve the electrochemical properties of LFP in LIBs, researchers have adopted a variety of strategies, including the nanocrystallization of grains[14,15], the coating of carbon-based materials[16-20] and single/double element doping[21-24]. Among the above-mentioned strategies, the doping of metal cations on the Fe site of LFP has been proved to be an effective method to improve its performance[25-31]. For instance, the doping of Mo, Nb, Mn and Co has been shown to improve the electronic conductivity of LFP[32]. However, the general influence of the doping of metal elements on the structural stability of LFP remains uncertain, despite its significant importance for the safety and stability of electrode materials and the overall battery. The effect of doping on the stability of LFP should be fully studied before the further large-scale application of doped LFP. The discharge capacity of solid-state prepared LFP decreased from 149 to 117 mAh·g⁻¹ with obvious cracks occurring after 60 cycles at 30 mA·g⁻¹, showing a significant reduction in electronic conductivity and capacity[33]. The degree of polarization and the number of cracks increase with the number of cycles due to the anisotropy, internal strain and the lithiation/delithiation process of lithium ions in LFP[33]. The crystal structure of LFP shows obvious anisotropy, and its elastic constant and bulk and shear elastic moduli show obvious changes during charging and discharging, which accelerate the collapse of its crystal structure[34].

As the earliest commercial cathode material of LIBs, doping at the Co site of $LiCoO_2$ (LCO) is known to play an active role in limiting its phase change and improving its cyclic stability[35]. In Fe-doped LCO ($LiFe_x$ $Co_{1-x}O_2$, $0 \leq x \leq 0.25$), there is no significant change in the symmetry of the crystal structure of LCO during charging and discharging[35]. In M-doped LCO ($LiM_{0.02}Co_{0.98}O_2$, M = Mo, V or Zr), the increased first-cycle irreversible capacity loss is 15, 22 and 45 mAh·g⁻¹ for Zr, Mo and V, respectively, and the cycling performance of all doped LCO models is inferior to that of pure LCO, illustrating that doping does not necessarily improve the electrochemical properties of the host material[36]. Mn-, Co-, Nb- and Mo-doped LFP models have relatively low formation energy and show improved mechanical stability[32]. The degree of anisotropy and the risk of microcracking in Mn-, Co-, Nb- and Mo-doped LFP models have been reduced[32]. Similar to doped LCO models, the symmetry and stability of the crystal structures of doped LFP models can change, so doping at the Fe site of LFP may play a positive role in its charge conduction capacity and structural stability. In general, the doping mechanisms of transition metals for LFP are still unclear.

Therefore, in order to unlock the effect of transition metal doping on the physical and chemical properties of LFP, particularly its stability and electronic conductivity, we establish models for all 3d, 4d and 5d transition metals doped in LFP (TM-LFP). We then compare and analyze their structural properties, band gaps, formation energies, elastic properties, anisotropies and lithiation/delithiation voltages using ab-initio computational screening based on six screening standards. Based on the results of this work, the TM-LFP models with high electronic conductivity, electrochemical stability and capacitive performance are identified and analyzed in detail.

COMPUTATIONAL METHODS

All the calculations of the TM-LFP models considered in this work were conducted using density functional theory (DFT) on the basis of the projector augmented wave (PAW) method and the Vienna Ab-initio Simulation Package (VASP)[37,38]. The general gradient approximation (GGA) method with the parameters of Perdew-Burke-Ernzerhof (PBE) was used for the exchange-correlation functionals in this work[39]. The

cutoff energy for the lattice optimization and property calculations was set as 500 eV for the expansion of the plane waves. Spin-polarized DFT was used to consider the possible magnetization in the doped models. The temperature width was set as 0.1 eV using the Gaussian electronic smearing method for the energy minimization of the electronic steps[40].

RESULTS AND DISCUSSION

In order to screen the TM-LFP structures with high electronic conductivity and structural stability, six indicators Supplementary Table 1, including the changes in lattice parameters and cell volumes, electronic properties, formation energies, elastic properties, anisotropies and lithiation/delithiation voltages, were considered in this work. The relative stability of the lattice structures and cell volumes are the premise for the excellent electrochemical properties of the corresponding structures. Small band gaps are a necessary prerequisite for electrode materials to have good electronic conductivity[41]. A lower dopant formation energy is the determining factor that doping models can be easier to successfully synthesize experimentally. Good elasticity is an important parameter for electrode materials to be able to restore their original appearance as much as possible after multiple charge-discharge cycles. High anisotropy makes the electrode material prone to cracks and reduces its cycle performance. The higher operating voltage of a particular electrode material allows the battery made with it to have a higher energy density. The six screening criteria selected for this work correspond to the key issues in the study of electrode materials, such as ease of synthesis (crystal structure properties and dopant formation energy), cyclic stability of the electrode (elastic properties and anisotropy), conductivity (band gap) and high energy and power density (high voltage). Therefore, the six indicators considered in this screening are practical and reasonable. The basic research contents and calculation methods are shown in Section 1 of the Supporting Information.

Screening for TM-LFP models with smaller cell volume changes

The cells of the LFP and TM-LFP models are shown in Figure 1A and B and Supplementary Figures 1-6, with the corresponding atomic fractional positions, atomic lattice constants and cell volumes presented in Figure 1C and D and Supplementary Tables 2-16. The optimized lattice constants of the considered LFP-based models (LFP and TM-LFP) are listed in Supplementary Table 17 and Supplementary Figure 7, which are consistent with some previously reported experimental and computational studies[32,42,43]. As can be seen from Figure 1C, both the lattice parameters and cell volumes of the TM-LFP models do not change significantly compared with LFP, with changes of less than 5.3% for lattice a, 2.1% for lattice b, 1.5% for lattice c and 8.4% for the cell volume [Supplementary Figures 7 and 8]. Therefore, the TM doping at the Fe site of LFP did not significantly change the crystal structure and volume of the LFP itself and compared with lattices b and c, the most varied lattice a is only 5.3% for the La-LFP models. It is noteworthy that the degree of change of the three cell parameters of LFP is not consistent by doping at the Fe site of LFP, showing that the introduction of dopants makes the stress inside the lattice of LFP change in the three directions to varying degrees, which will be studied in the following sections (i.e., screening for higher elastic properties of TM-LFP and screening for higher isotropy of TM-LFP).

Generally, the TM-LFP models with TM elements in the groups of IIIB to IVB and IB to IIB induce the greatest changes in the LFP lattice, as presented by the red and orange areas of Figure 1E, which may be because these TMs have the outermost electronic structure that differs significantly from Fe in group VIII. Depending on the extent of the cell volume changes, sixteen TM-LFP models with volume changes of less than 2% relative to LFP were filtered out, as shown in the yellow and white areas in Figure 1E. The three TM-doped LFP structures with the smallest cell volume variations are Os-LFP, V-LFP and Zn-LFP, as shown in the right-bottom corner of Figure 1E.
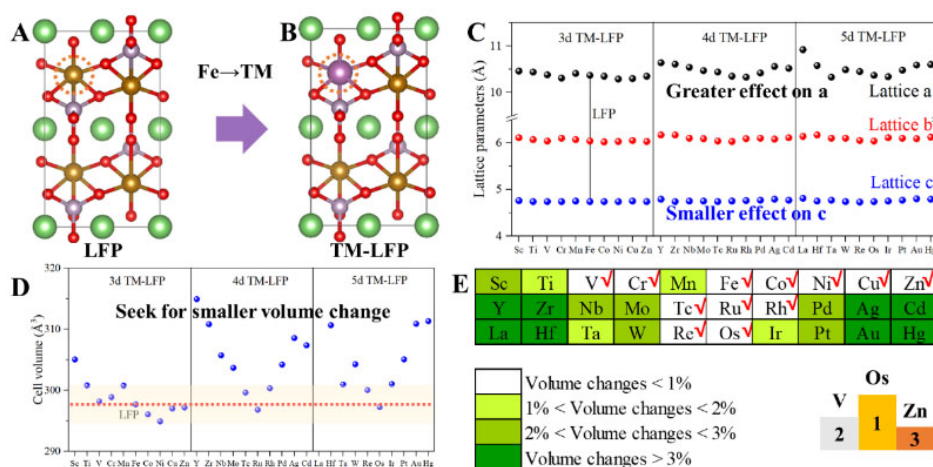
Figure 1. Screening for smaller volume changes of TM-LFP. A: Cell structure of LFP. B: Cell structure of TM-LFP with a TM doped at Fe site. C: Lattice parameters of LFP and TM-LFP, where doping has a greater effect on the length of the "a" direction than the "c" direction. D: Cell volumes of LFP and TM-LFP. The light-yellow region denotes TM-doped structures with small volume changes. E: Changes in cell volume of TM-LFP compared with LFP and three structures with minimal volume variations, where the darker the color, the greater the volume of TM-LFP changes from LFP. LFP: LiFePO$_4$; TM-LFP: Transition metal-doped LFP.

**Screening for TM-LFP models with smaller band gaps**

According to the calculation results of the parameters set by this work, the band gap of LFP is 0.42 eV, and the replacement of TM atoms at the Fe site of LFP can effectively reduce the band gap of LFP, except for the doping of Zn atoms, as shown in Figures 2A-C and Supplementary Table 18. To specify the effect of TM doping on the electronic structure of LFP, we chose Mn to explain the Fe site doping of LFP as an example, as shown in Figure 2A. The Mn s and p electron orbitals have no electronic states in the range of -5 to 5 eV. The Mn d orbital has obvious electronic states at three positions of -1.3, 0.3 and 1.8 eV, which has an obvious regulating effect on the total electronic DOS of LFP.

Overall, all the 3d, 4d and 5d TM dopants, except for Zn and Tc, significantly reduced the band gap of LFP, which dropped below 0.1 eV, as shown in Figures 2B and C. The values of the band gap of each model considered in this work are shown in Supplementary Table 18 and Supplementary Figure 8. The structural models of band gaps of less than 0.05 eV are considered feasible in the white and yellow areas of Figure 2D and Supplementary Figure 9A. There is a strong linear relationship between the electronic structure (d-band) of the dopant and the total electronic DOS, as shown in Supplementary Figure 9B. The three TM-doped LFP models with the smallest band gaps are Sc-LFP, Co-LFP and Re-LFP, as shown in the right-bottom corner of Figure 2D.

Screening for TM-LFP models with lower formation energy

Dopant formation energy is an important indicator to theoretically predict the possibility of the formation of a doped structure and the smaller its corresponding value, the easier it is to form experimentally[44-46]. The formation energy of a reaction process that is greater (lower) than 0 eV indicates that the corresponding reaction process is endothermic (exothermic). Formation energy is achieved by calculating the energy differences before and after the formation of the research system, as shown in Equation (1)[47]:

$$E_{formation} = E_{total} - E_{pure} - \sum_i n_i \mu_i \tag{1}$$
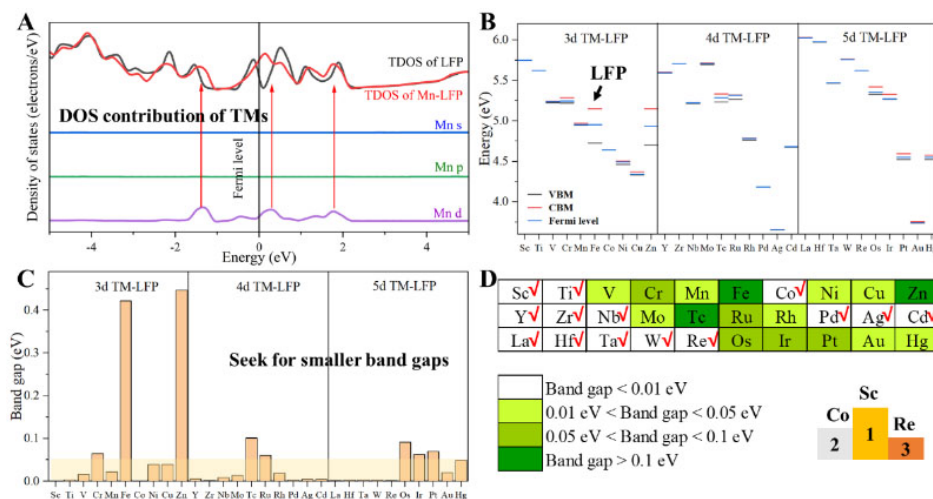
Figure 2. Screening for smaller band gaps of TM-LFP. A: Total electronic density of states (DOS) of LFP and Mn-LFP (taking Mn as an example) and projected DOS of Mn s, p and d states in Mn-LFP, where the Fermi levels of LFP and Mn-LFP are shifted to 0 eV. The DOS near the Fermi level mainly consists of Mn d states. B: Valence band maxima, conduction band minima and Fermi levels of all 3d, 4d and 5d TM-doped LFP models. C: Band gaps of LFP and TM-LFP. The light-yellow region denotes TM-doped structures with smaller band gaps and higher electronic conductivity. D: Band gaps of all 3d, 4d and 5d TM-doped LFP models compared with LFP, where the darker the color, the greater the band gaps. LFP: LiFePO$_4$; TM-LFP: Transition metal-doped LFP.

where E_{total} is the total energy of a defective or impurity-containing system, E_{pure} is the total energy of the pure system. n_i is the quantity of atoms of type i that have been added to ($n_i > 0$) or removed from ($n_i < 0$) the pure system and μ_i is the chemical potential of the corresponding added or removed atoms.

Specifically, for the TM-doped LFP models considered in this work, the corresponding dopant formation energy can be calculated by Equation (2):

$$E_{formation} = E_{LiM_xFe_{1-x}PO_4} - E_{LiFePO_4} + nE_{Fe} - nE_M \qquad (2)$$

where $E_{LiM_xFe_{1-x}PO_4}$ is the total energy of the TM-doped LFP model, E_{LiFePO_4} is the total energy of pure LFP, E_{Fe} and E_M are the chemical potentials of Fe and the doped TM atoms, respectively, and $n = 1$ (one Fe atom of LFP has been replaced by one particular TM atom) in this work. The formation energies of the TM-doped LFP models are illustrated in Figure 3A and Supplementary Table 19. The TM-LFP models with TM atoms in the IIIB to VIB groups usually exhibit a formation energy lower than 0 eV, while the models with TM atoms in the VIIB to IIB groups usually exhibit a formation energy larger than 0 eV. According to previous reports, structures with a formation energy of less than 2 eV are relatively easy to form experimentally[44,45]. Therefore, the LFP structures doped by TMs in the IIIB to VIB groups are relatively easier to form. The formation energies of LFP doped by Zn, Pd, Ag, Cd, Pt, Au and Hg are greater than 2 eV, indicating that these materials are difficult to form by doping in experiments, while others are possible [Supplementary Figure 10]. The formation energy of Sc-, Ti-, V-, Cr-, Y-, Zr-, Nb-, Mo-, Ru-, La-, Hf-, Ta- and W-doped LFP are less than 0 eV, which are very easy to form experimentally by doping.

Therefore, the structural models of formation energies less than 2 eV, in the orange, yellow and white areas of Figure 3B, are considered feasible in this work. The structures of the three TM-doped LFPs with the lowest doping formation energies are Y-LFP, Hf-LFP and La-LFP, as shown in the right-bottom corner of Figure 3B.
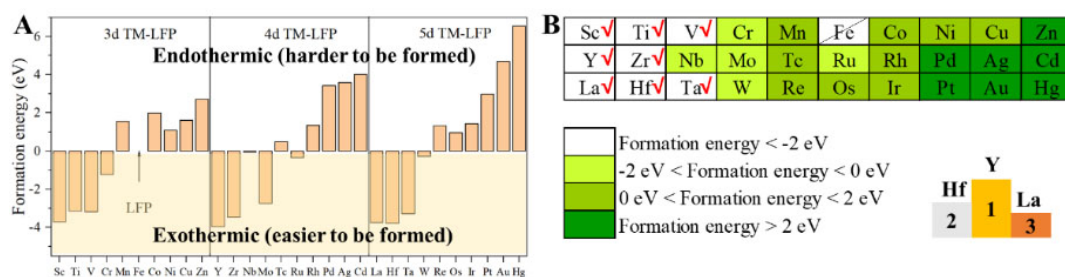
Figure 3. Screening for smaller dopant formation energy of TM-LFP. A: Formation energies of LFP and TM-LFP. The white and light-yellow areas correspond to the elements with endothermic and exothermic formation, respectively. B: Classification of formation energy of TM-LFP compared with LFP, where the darker the color, the larger the formation energy. LFP: LiFePO$_4$; TM-LFP: Transition metal-doped LFP.

Screening for TM-LFP models with higher elastic properties

The stability of electrode materials, especially elasticity properties, is of great significance in determining the electrochemical properties of LIBs[48-50]. Poor material stability is usually demonstrated by phase change and degradation, in which the main impact is the cycling properties of the assembled LIBs by the electrode material[51]. Therefore, it is necessary to study the stability of materials by theoretical calculations, with many relevant research works having been carried out[32,52-55].

In this work, we calculated the elasticity of all 3d, 4d and 5d TM-doped LFP models. The stiffness coefficient (c_{ij}) and compliance coefficient (s_{ij}) are used to calculate the elastic properties of the above materials, which are intrinsic properties. The c_{ij} and s_{ij} of a single degree of freedom are reciprocal to each other[32]. In materials with orthorhombic crystal structures (like LFP), c_{11}, c_{22} and c_{33} correspond to linear compressibility in the X, Y and Z directions, respectively, shown in Figure 4A, while c_{44}, c_{55} and c_{66} correspond to the shear strengths in {100}, {010} and {001}, respectively, shown in Figure 4B. In contrast, when the materials are elongated longitudinally, they interact in the lateral direction. c_{12}, c_{13} and c_{23} indicate the interactions between the X and Y, X and Z, and X and Z directions, respectively.

The calculated c_{ij} are shown in Supplementary Tables 20-50. It can be seen that, with the introduction of TMs, the original orthorhombic structure of LFP undergoes a slight deformation, which we deem the pseudo-orthorhombic structure. This explains the reason why the c_{ij} results we calculated are slightly different from standard LFP. The stability criteria for orthorhombic crystal structures are shown by Equations (3-5):

$$c_{11} > 0, c_{22} > 0, c_{33} > 0, c_{44} > 0, c_{55} > 0, c_{66} > 0 \qquad (3)$$

$$c_{11} + c_{22+}c_{33} + 2(c_{12} + c_{13+}c_{23}) > 0 \qquad (4)$$

$$c_{11} + c_{22} - 2c_{12} > 0, \ c_{11} + c_{33} - 2c_{13} > 0, \ c_{22} + c_{33} - 2c_{23} > 0 \qquad (5)$$

Based on the results of our calculations and with reference to the stability criteria in Equations (3-5), we have summarized the c_{ij} corresponding to the LFP doped with all 3d to 5d transition metals, as shown in Figure 4C. The Tc-LFP model does not meet the stability criteria in the above formula. Overall, the linear compressibility-related coefficients of the above materials are greater than the shear-dependent coefficients, which indicates that they are more sensitive to shear strain. The linear compressibility of TM-LFP in X is shown in Supplementary Figure 11, which has been improved with TM = Os, Mo, Ta, Ni, Ru and Zn. The
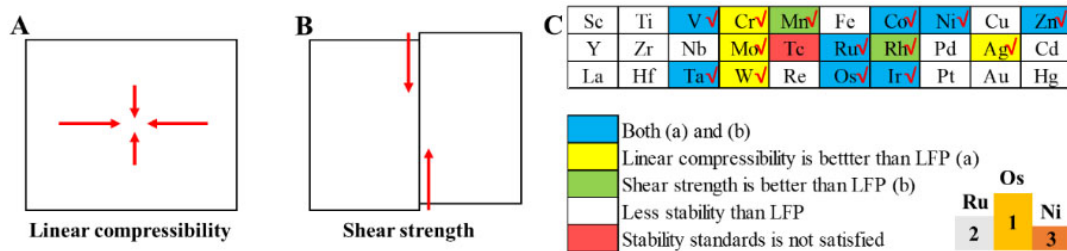
Figure 4. Screening for higher elastic properties of TM-LFP. A: Model of linear compressibility. B: Model of shear strength. C: Structural stabilities of TM-LFP and LFP considered by stability standards, linear compressibility and shear strength. Models with higher stability are shown in yellow, green and blue. LFP: $LiFePO_4$.

linear compressibility of TM-LFP in Y is shown in Supplementary Figure 12, which has been improved with TM = Ir, Os, Ta, Zn, Ni, Ru, Ag and W. The linear compressibility of TM-LFP in Z is shown in Supplementary Figure 13, which has been improved with TM = Co, Os, Cr and V. The interaction between X and Y is shown in Supplementary Figure 14, which has been improved with TM = Ru, Os, Zn, Ir and Ni. The interaction between Y and Z is shown in Supplementary Figure 15, which has been improved with TM = Ru, Ta, V, Co, Os, Ni, Tc and Mn. The interaction between Z and X is shown in Supplementary Figure 16, which has been improved with TM = Ru, Os, Ni and Rh.

The summary of the linear compressibility of the TM-LFP models is shown in Supplementary Figure 17, in which the yellow area indicates the models with higher linear compressibility than pure LFP and X, Y and Z indicate the directions of particular TM-LFP models. The summary of the shear strength of the TM-LFP models is shown in Supplementary Figure 18, in which the green area indicates the models with higher shear strength than pure LFP and the XY, YZ and ZX indicate the directions of particular TM-LFP models.

Compared with pure LFP, the stability of Sc-, Ti-, Cu-, Y-, Zr-, Nb-, Pd-, Ag-, Cd-, La-, Hf-, Re-, Pt-, Au- and Hg-doped LFP decreased, as shown in the white area of Figure 4C. This may be because the valence electron structures of these TM atoms differ greatly from Fe. For linear compressibility, V-, Cr-, Co-, Ni-, Zn-, Mo-, Ru-, Ta-, W-, Os- and Ir-doped LFP are greater than that of pure LFP, indicating an increase in linear compressibility after doping, as shown in the yellow and blue areas of Figure 4C. For shear strength, Mn-, Co-, Ni-, Zn-, Ru-, Rh-, Ta-, Os- and Ir-doped LFP are greater than that of pure LFP, indicating an increase in shear strength after doping, as shown in the green and blue areas of Figure 4C.

It is noteworthy that for Co-, Ni-, Zn-, Ru-, Ta-, Os- and Ir-doped LFP, compared with pure LFP, both their linear compressibility and shear intensity increase. Therefore, for LIBs, they can be considered as promising dopants for LFP, as shown in the blue area of Figure 4C. Through the above analysis, considering the linear compressibility and shear strength of the TM-LFP models, the three TM-doped LFP models with the best elastic performance are Os-LFP, Ru-LFP and Ni-LFP, as shown in the right-bottom corner of Figure 4C.

Screening for TM-LFP models with higher isotropy

According to relevant experimental reports, after dozens of charge and discharge cycles, cracks appear in pure and doped LFP[33,34]. The appearance of cracks plays a very important role in the attenuation of the electrochemical properties of the electrode material, which is closely related to the anisotropy of the electrodes[56-59]. The more anisotropic an electrode material is, the more likely it is to cause changes in its own structure during cycling, resulting in cracks on the surface of the electrode particles. Therefore, screening electrode materials with high isotropy is beneficial in reducing the occurrence of cracks in the circulation of electrode materials. The anisotropy of the shear modulus for orthorhombic lattices is

presented in Equations (6-8) as follows:

$$A_1 = 4c_{44}/(c_{11} + c_{33} - 2c_{13}) \tag{6}$$

$$A_2 = 4c_{55}/(c_{22} + c_{33} - 2c_{23}) \tag{7}$$

$$A_1 = 4c_{66}/(c_{11} + c_{22} - 2c_{12}) \tag{8}$$

where A_1, A_2 and A_3 represent the anisotropy shear moduli of the <010> and <011> directions of {100} planes, the <001> and <100> directions of {010} planes and the <110> and <010> directions of {001} planes, respectively. The calculated results of anisotropy shear moduli of all the TM-LFP models are shown in Supplementary Table 51. It is noteworthy that the deviation of A_i from 1 shows the degree of anisotropy, shown in Figure 5A, and the value of A_i close to 1 indicates the extent of isotropy for a particular material, shown in Figure 5B. The above-described adjustment of anisotropy can be achieved by the selective doping of Fe sites in LFP.

The anisotropy shear moduli of the <010> and <011> directions of the {100} planes (A_1) of the TM-LFP models are shown in Supplementary Figure 19, in which the corresponding anisotropy of Ru-LFP, Ir-LFP and Os-LFP models is minimal. The anisotropy shear moduli of the <001> and <100> directions of the {010} planes (A_2) of the TM-LFP models are shown in Supplementary Figure 20, in which the corresponding anisotropy of Mn-LFP, W-LFP and La-LFP is minimal. The anisotropy shear moduli of the <110> and <010> directions of the {001} planes are shown in Supplementary Figure 21, in which the corresponding anisotropy of Cr-LFP, Ru-LFP and La-LFP is minimal.

In this work, the anisotropy (A) of a particular material is obtained by summing A_i in three different directions, as shown in Equation (9):

$$A = \sum |A_i\text{-}1| \tag{9}$$

where i = 1, 2 or 3. To compare the isotropy of models of different TM-doped LFP models (A_{TM}) with the anisotropy of the LFP itself (A_{LFP}), we use the difference (I_{TM}) between the two models as an indicator, which can be calculated by Equation (10):

$$I_{TM} = A_{LFP}\text{-}A_{TM} \tag{10}$$

where $I_{TM} < 0$ indicates a model with higher anisotropy than pure LFP. Our aim is to find TM-doped LFP models with reduced anisotropy ($I_{TM} > 0$). Based on the comprehensive consideration of the calculated A_i, the doping effect of TMs on the anisotropy of LFP is summarized in Figure 5C and Supplementary Figure 22. The isotropy of LFP is enhanced by the doping of Ti, V, Mn, Ni, Nb, Ru, Rh, Cd, La, W and Os, as shown in the yellow area of Figure 5C, while other TMs are not, as shown in the blue area of Figure 5C. The increase of isotropy will reduce the possibility of cracks to a certain extent, which plays an important role in improving electrochemical properties. Through the above analysis and Supplementary Figure 22, the three TM-doped LFP models with the highest isotropic properties are Ru-LFP, W-LFP and Os-LFP, as shown in the right-bottom corner of Figure 5C.
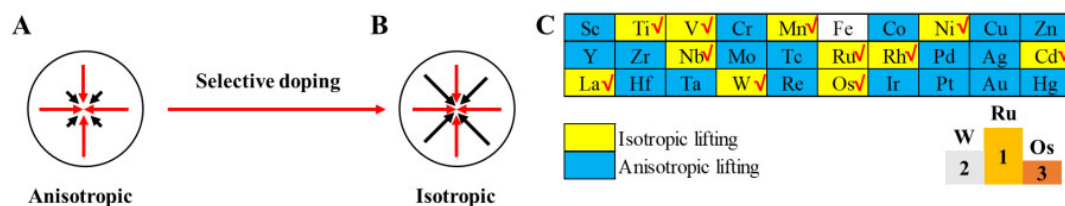
Figure 5. Screening for higher isotropy of TM-LFP. Models of (A) anisotropy (before doping) and (B) isotropy (after selective doping). (C) Anisotropies of TM-LFP compared with LFP.

Screening for higher operating voltages

High-voltage LIBs will have a larger market space in the future due to their higher energy density, and increasing the operating voltage of the cathode material has a positive significance for increasing the operating voltage of LIBs. The lithiation/delithiation voltage (U) of TM-LFP cathodes can be calculated by Equation (11):

$$U = \frac{-\left(E_{TM\text{-}LiFePO_4} - E_{TM\text{-}Li_{1-x}FePO_4} - xE_{Li}\right)}{xe} \tag{11}$$

In order to increase the operating voltage of LFP by TM doping, the lithiation/delithiation voltages of all the 3d, 4d and 5d TM-doped LFP models are calculated, as shown in Figure 6A and Supplementary Table 52. By selectively doping TMs in LFP, significant lithiation/delithiation voltage increases (especially greater than 4V) can be seen, as shown in the Supplementary Figure 23 and the yellow area of Figure 6A. In order to analyze the effect of the doping of different TM elements more clearly on the lithiation/delithiation voltage of LFP, we divided the voltage range into three parts with 3 and 4 V, as shown in Figure 6B. The red area in Figure 6B donates the TM-LFP models with lithiation/delithiation voltages theoretically lower than 3.0 V, which will not be considered in the further analysis due to the relatively smaller voltage. In the white region of Figure 6A, the lithiation/delithiation voltage corresponding to the doped LFP model with five TMs theoretically exceeds 4 V, which has the advantage of increasing the LFP voltage significantly. The three TM-doped LFP models with the highest lithiation/delithiation are Ag-LFP, Cu-LFP and Pd-LFP, as shown in the right-bottom corner of Figure 6B.

Suitable TM doping for LFP

In fact, when screening the models of TM-doped LFP, multiple factors need to be considered simultaneously rather than individually. In order to identify the TM-LFP cathode materials with excellent performance, through the analysis of the previous six parts, we established the screening criteria shown in Table 1 in this work. Finally, based on the above screening criteria, we analyzed 30 TM-LFP models and the results are shown in Figures 7 and 8. Overall, the V-, Mn-, Ni-, Rh- and Os-doped LFP models show relatively excellent electrochemical performance, which meets the above screening criteria. It is noteworthy that the V-LFP model is the easiest to form and has a minimal band gap. In contrast, Ni-LFP has the highest lithiation/delithiation voltage.

CONCLUSIONS

Although LFP is one of the most attractive cathode materials for lithium-ion batteries, the large-scale applications of LFP have been limited by its relatively low electronic and ionic conductivity. It is an effective strategy to improve the electronic and ionic conductivity electrode materials by doping. In this work, in order to compare the electrochemical properties of 3d, 4d and 5d transition metal-doped LFP (TM-LFP), we used the method of first-principles calculations to theoretically analyze all doped structures from the

Table 1. Screening criteria for TM-LFP models in this work

No.	Items	Screening criteria
(1)	Cell volume change	Less than 2% compared with LFP
(2)	Band gap	Less than 0.1 eV
(3)	Doping formation energy	Less than 2 eV
(4)	Linear compressibility and shear strength	Both linear compressibility and shear strength higher than LFP
(5)	Isotropy	Higher than LFP
(6)	Lithiation/delithiation voltage	Higher than 3 eV

LFP: $LiFePO_4$.
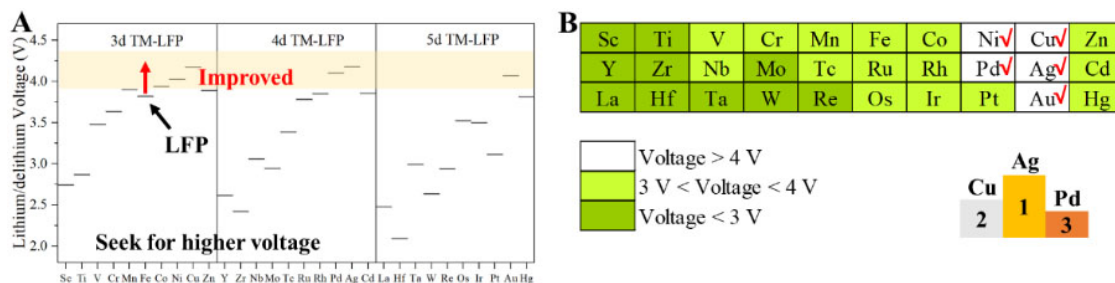
Figure 6. Screening for higher operating voltages. A: Lithiation/delithiation voltages of TM-LFP and LFP, where the white area shows the corresponding models with higher lithiation/delithiation voltages compared with LFP. B: Classification of lithiation/delithiation voltages of TM-LFP and LFP, where the darker the color, the higher the lithiation/delithiation voltages. LFP: $LiFePO_4$.
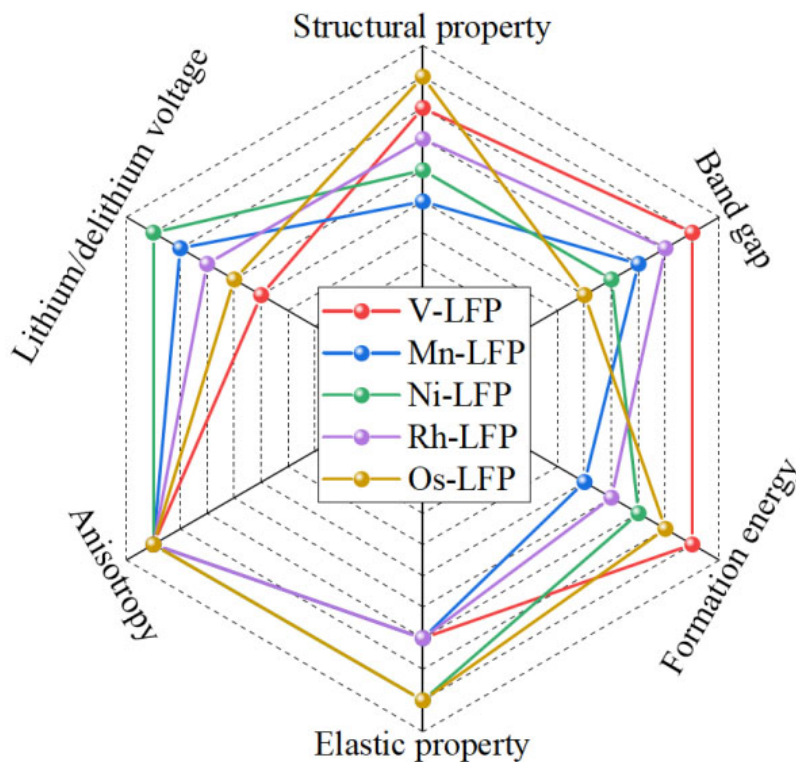
Figure 7. Radar diagram of TM-doped LFP models with excellent electrochemical performance screened from a comparison of the six screen standards. LFP: $LiFePO_4$.
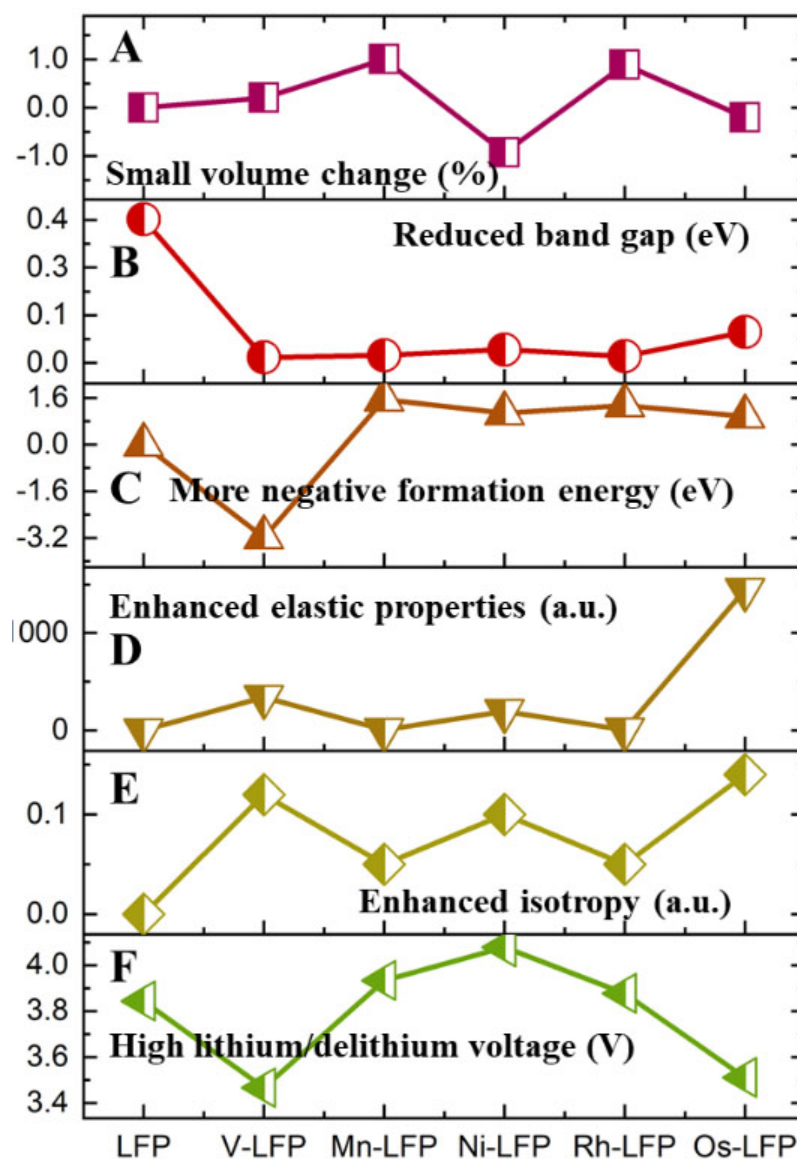
Figure 8. Performance comparison of five TM-LFP models with excellent electrochemical properties based on the screening criteria in this work. A: Cell volume change. B: Band gap. C: Dopant formation energy. D: Elastic properties (including linear compressibility and shear strength). E: Isotropy. F: Lithiation/delithiation voltage. LFP: $LiFePO_4$.

perspectives of structural properties, band gaps, formation energy, elastic properties, anisotropy and lithiation/delithiation voltage. According to our screening results, the V-, Mn-, Ni-, Rh- and Os-doped LFP structures have good electrochemical properties and can be used as cathode materials for LIBs. Moreover, the reasons for the inherent principle of the above materials showing excellent electrochemical properties are presented.

DECLARATIONS
Authors' contributions
Conception of the study and wrote the manuscript: Zhang B, Wang X, He X

Conflicts of interest
All authors declared that there are no conflicts of interest.

Ethical approval and consent to participate
Not applicable.

Consent for publication
Not applicable.

REFERENCES

1. Padhi AK, Nanjundaswamy KS, Goodenough JB. Phospho-olivines as positive-electrode materials for rechargeable lithium batteries. *J Electrochem Soc* 1997;144:1188-94. DOI
2. Q; Advanced Batteries and Materials Engineering Research Center, Guizhou Light Industry Technical College, Guiyang 550025, China. Combined first-principles and experimental studies of a V- doped LiFePO$_4$/C composite as a cathode material for lithium-ion batteries. *Int J Electrochem Sci* 2021. DOI
3. Zhang X, Ge X, Shen Z, et al. Green water-based binders for LiFePO$_4$ /C cathodes in Li-ion batteries: a comparative study. *New J Chem* 2021;45:9846-55. DOI
4. Wang Y, Zhang J, Xue J, Ke X, Liang G. LiFePO$_4$/C composites with high compaction density as cathode materials for lithium-ion batteries with high volumetric energy density. *Ionics* 2021;27:4687-94. DOI
5. Song Y, Xie B, Song S, et al. Regeneration of LiFePO$_4$ from spent lithium-ion batteries via a facile process featuring acid leaching and hydrothermal synthesis. *Green Chem* 2021;23:3963-71. DOI
6. Huang X, He X, Jiang C, Tian G, Liu Y. Reaction mechanisms on solvothermal synthesis of nano LiFePO$_4$ crystals and defect analysis. *Ind Eng Chem Res* 2017;56:10648-57. DOI
7. Garay-marín JD, Quiroga-gonzález E, Garza-tovar LL, et al. High-performing li-ion battery with "two cathodes in one" of sulfur and LiFePO$_4$ by strategies of mitigation of polysulfide shuttling. *Batteries & Supercaps* 2021;4:359-67. DOI
8. Cui Z, Guo X, Ren J, et al. Enhanced electrochemical performance and storage mechanism of LiFePO$_4$ doped by Co, Mn and S elements for lithium-ion batteries. *Electrochimica Acta* 2021;388:138592. DOI
9. Cheng Q, Zhao X, Yang G, et al. Recent advances of metal phosphates-based electrodes for high-performance metal ion batteries. *Energy Stor Mater* 2021;41:842-82. DOI
10. Zhong Z, Chen L, Zhu C, Ren W, Kong L, Wan Y. Nano LiFePO$_4$ coated Ni rich composite as cathode for lithium ion batteries with high thermal ability and excellent cycling performance. *J Power Sources* 2020;464:228235. DOI
11. Nie Z, Liu Y, Yang L, Li S, Pan F. Construction and application of materials knowledge graph based on author disambiguation: revisiting the evolution of LiFePO$_4$. *Adv Energy Mater* 2021;11:2003580. DOI
12. Sifuba S, Willenberg S, Feleni U, Ross N, Iwuoha E, Khabashesku V. Electrochemical analysis of architecturally enhanced LiFe$_{0.5}$Mn$_{0.5}$PO$_4$ multiwalled carbon nanotube composite. *J Nanotechnol* 2021;2021:1-8. DOI
13. Sifuba S, Willenberg S, Feleni U, Ross N, Iwuoha E. Electrochemical analysis of architecturally enhanced LiFe$_{0.5}$Mn$_{0.5}$PO$_4$ multi-

    walled carbon nanotube composite. *JNanoR* 2021;66:1-11. DOI

14. Adepoju AA, Williams QL. High C-rate performance of LiFePO$_4$/carbon nanofibers composite cathode for Li-ion batteries. *Curr Appl Phys* 2020;20:1-4. DOI

15. Bazzi K, Dhindsa KS, Dixit A, et al. Nanostructured high specific capacity C-LiFePO$_4$ cathode material for lithium-ion batteries. *J Mater Res* 2012;27:424-30. DOI

16. Tian X, Chen W, Jiang Z, Jiang Z. Porous carbon-coated LiFePO$_4$ nanocrystals prepared by in situ plasma-assisted pyrolysis as superior cathode materials for lithium ion batteries. *Ionics* 2020;26:2715-26. DOI

17. Wang C, Yuan X, Tan H, et al. Three-dimensional carbon-coated LiFePO$_4$ cathode with improved li-ion battery performance. *Coatings* 2021;11:1137. DOI

18. Yang G, Jiang CY, He XM, Ying JR, Gao J. Preparation of Li$_3$V$_2$ (PO$_4$)$_3$/LiFePO$_4$ composite cathode material for lithium ion batteries. *Ionics* 2013;19:1247-53. DOI

19. Ren J, Pu W, He X, Jiang C, Wan C. A carbon-LiFePO$_4$ nanocomposite as high-performance cathode material for lithium-ion batteries. *Ionics* 2011;17:581-6. DOI

20. Gao J, Li JJ, He XM, Jiang CY, Wan CR. Synthesis and electrochemical characteristics of LiFePO$_4$/C cathode materials from different precursors. *Int J Electrochem Sci* 2011;6(7):2818-2825. Available from: http://www.electrochemsci.org/papers/vol6/6072818.pdf.

21. Gao Y, Xiong K, Zhang H, Zhu B. Effect of Ru doping on the properties of LiFePO$_4$/C cathode materials for lithium-ion batteries. *ACS Omega* 2021;6:14122-9. DOI PubMed PMC

22. Liu Z, Huang X, Wang D. First-principle investigations of N doping in LiFePO$_4$. *Solid State Commun* 2008;147:505-9. DOI

23. Yolun A, Altin E, Altundag S, Arshad M, Abbas SM, Altin S. Investigation of structural and electrochemical performance of Ru-substituted LiFePO$_4$ cathode material: an improvement of the capacity and rate performance. *J Mater Sci: Mater Electron* 2022;33:6670-80. DOI

24. Zhang L, Zeng D. Aluminium behaviour in preparation process of lithium iron phosphate and its effects on material electrochemical performance. *J Mater Res Technol* 2021;15:3575-84. DOI

25. Bai J, Hong J, Chen H, Graetz J, Wang F. Solvothermal synthesis of LiMn$_{1-}$. x ;119:2266-76. DOI

26. Li JG, Zhao PX, Duan WL, Wang L, Li JJ, He XM. Hydrothermal synthesis of well-dispersed LiMn$_{0.7}$Fe$_{0.3}$PO$_4$/C nanocrystalline cathodes for lithium-ion batteries. *Int J Electrochem Sci* 2015;10(9):7371-7379. Available from: http://www.electrochemsci.org/papers/vol10/100907371.pdf.

27. Ye F, Wang L, He X, et al. Solvothermal synthesis of nano LiMn$_{0.9}$Fe$_{0.1}$PO$_4$: reaction mechanism and electrochemical properties. *J Power Sources* 2014;253:143-9. DOI

28. Yang G, Jiang C, He X, Ying J, Cai F. Preparation of V-LiFePO$_4$ cathode material for Li-ion batteries. *Ionics* 2012;18:59-64. DOI PubMed

29. Wang L, Zhang LW, Li JJ, Gao J, Jiang CY, He XM. First-principles study of doping in LiMnPO$_4$. *Int J Electrochem Sci* 2012;7(4):3362-3370. Available from: http://www.electrochemsci.org/papers/vol7/7043362.pdf.

30. Ying J, Lei M, Jiang C, et al. Preparation and characterization of high-density spherical Li$_{0.97}$Cr$_{0.01}$FePO$_4$/C cathode material for lithium ion batteries. *J Power Sources* 2006;158:543-9. DOI

31. Trinh DV, Nguyen MTT, Dang HTM, et al. Hydrothermally synthesized nanostructured LiMn$_x$Fe$_{1-x}$PO$_4$ (x = 0-0.3) cathode materials with enhanced properties for lithium-ion batteries. *Sci Rep* 2021;11:12280. DOI PubMed PMC

32. Zhang D, Wang J, Dong K, Hao A. First principles investigation on the elastic and electronic properties of Mn, Co, Nb, Mo doped LiFePO$_4$. *Comput Mater Sci* 2018;155:410-5. DOI

33. Wang D, Wu X, Wang Z, Chen L. Cracking causing cyclic instability of LiFePO$_4$ cathode material. *J Power Sources* 2005;140:125-8. DOI

34. Maxisch T, Ceder G. Elastic properties of olivine LixFePO4 from first principles. *Phys Rev B* 2006:73. DOI

35. Kobayashi H, Shigemura H, Tabuchi M, et al. Electrochemical properties of hydrothermally obtained LiCo[sub 1−x]Fe[sub x]O[sub 2] as a positive electrode material for rechargeable lithium batteries. *J Electrochem Soc* 2000;147:960. DOI

36. Needham S, Wang G, Liu H, Drozd V, Liu R. Synthesis and electrochemical performance of doped LiCoO$_2$ materials. *J Power Sources* 2007;174:828-31. DOI

37. Kresse G, Furthmüller J. Efficient iterative schemes for ab initio total-energy calculations using a plane-wave basis set. *Phys Rev B Condens Matter* 1996;54:11169-86. DOI PubMed

38. Hafner J. Ab-initio simulations of materials using VASP: density-functional theory and beyond. *J Comput Chem* 2008;29:2044-78. DOI PubMed

39. Perdew JP, Burke K, Ernzerhof M. Generalized Gradient Approximation Made Simple. *Phys Rev Lett* 1996;77:3865-8. DOI PubMed

40. Barma M. Gaussian smearing of spin weight functions in models of phase transitions. *J Phys A: Math Gen* 1983;16:L745-50. DOI

41. Yang L, Tian Y, Chen J, et al. A high-rate capability LiFePO$_4$ /C cathode achieved by the modulation of the band structures. *J Mater Chem A* 2021;9:24686-94. DOI

42. Avilov A, Lepeshov G, Pietsch U, Tsirelson V. Multipole analysis of the electron density and electrostatic potential in germanium by high-resolution electron diffraction. *J Phys Chem Solids* 2001;62:2135-42. DOI

43. Shi S, Liu L, Ouyang C, et al. Enhancement of electronic conductivity of LiFePO$_4$ by Cr doping and its identification by first-principles calculations. *Phys Rev B* 2003:68. DOI

44. Zhang B, Peng Z, Song L, Wu X, Fu X. Computational screening toward quantum capacitance of transition-metals and vacancy

doped/co-doped graphene as electrode of supercapacitors. *Electrochimica Acta* 2021;385:138432. DOI

45. Zhang B, Fu X, Song L, Wu X. Computational screening toward hydrogen evolution reaction by the introduction of point defects at the edges of group IVA monochalcogenides: a first-principles study. *J Phys Chem Lett* 2020;11:7664-71. DOI PubMed

46. Xu CH, Wang L, He XM, Luo J, Shang YM, Wang JL. Formation mechanism and growth habit of olivine-$LiFePO_4$ materials by hydrothermal synthesis. *Int J Electrochem Sci* 2016;11(2):1558-1567. Available from: http://www.electrochemsci.org/papers/vol11/110201558.pdf.

47. de Walle CG, Neugebauer J. First-principles calculations for defects and impurities: Applications to III-nitrides. *Journal of Applied Physics* 2004;95:3851-79. DOI

48. Ko M, Chae S, Jeong S, Oh P, Cho J. Elastic a-silicon nanoparticle backboned graphene hybrid as a self-compacting anode for high-rate lithium ion batteries. *ACS Nano* 2014;8:8591-9. DOI PubMed

49. Chang B, Kim J, Cho Y, et al. Highly elastic binder for improved cyclability of nickel-rich layered cathode materials in lithium-ion batteries. *Adv Energy Mater* 2020;10:2001069. DOI

50. Zhang W, Hu J, Guo Y, et al. Tin-nanoparticles encapsulated in elastic hollow carbon spheres for high-performance anode material in lithium-ion batteries. *Adv Mater* 2008;20:1160-5. DOI

51. Chen Y, Wang L, Anwar T, et al. Application of galvanostatic intermittent titration technique to investigate phase transformation of $LiFePO_4$ nanoparticles. *Electrochimica Acta* 2017;241:132-40. DOI

52. Zhang B, Fu X, Song L, Wu X. Surface selectivity of Ni_3S_2 toward hydrogen evolution reaction: a first-principles study. *Phys Chem Chem Phys* 2020;22:25685-94. DOI PubMed

53. Güler E, Güler M, Uğur Ş, Uğur G. DFT aspects of the elastic, mechanical, magnetic, thermodynamic and optical properties of Ce_3 XY perovskites. *Philos Mag* 2022;102:244-63. DOI

54. Khanzadeh M, Alahyarizadeh G. A DFT study on pressure dependency of TiC and ZrC properties: interconnecting elastic constants, thermodynamic, and mechanical properties. *Ceram Int* 2021;47:9990-10005. DOI

55. Chibani S, Chami N, Arbouche O, Amara K, Kafi A. Structural, elastic, electronic and transport properties of CoVX (X = Ge and Si) compounds: a DFT prediction. *Computational Condensed Matter* 2020;24:e00475. DOI

56. Hashigami S, Kato Y, Yoshimi K, et al. Effect of lithium silicate addition on the microstructure and crack formation of $LiNi_{0.8}Co_{0.1}Mn_{0.1}O_2$ cathode particles. *ACS Appl Mater Interfaces* 2019;11:39910-20. DOI PubMed

57. Trevisanello E, Ruess R, Conforto G, Richter FH, Janek J. Polycrystalline and single crystalline NCM cathode materials-quantifying particle cracking, active surface area, and lithium diffusion. *Adv Energy Mater* 2021;11:2003400. DOI

58. Pang P, Tan X, Wang Z, et al. Crack-free single-crystal $LiNi_{0.83}Co_{0.10}Mn_{0.07}O_2$ as cycling/thermal stable cathode materials for high-voltage lithium-ion batteries. *Electrochimica Acta* 2021;365:137380. DOI

59. Kumberg J, Müller M, Diehm R, et al. Drying of lithium-ion battery anodes for use in high-energy cells: influence of electrode thickness on drying time, adhesion, and crack formation. *Energy Technol* 2019;7:1900722. DOI